Electronic Supplementary Material (ESI) for Materials Advances.

Metal cation s lone-pairs increase octahedral tilting instabilities in halide perovskites

Lingyuan Gao[+],[1] Lena Yadgarov[+],[2] Rituraj Sharma,[2] Roman Korobko,[2]
Kyle McCall,[3] Douglas H. Fabini,[4] Constantinos C. Stoumpos,[5]
Mercouri G. Kanatzidis,[3] Andrew M. Rappe,[1] and Omer Yaffe[2,*]

[1]*Department of Chemistry, University of Pennsylvania, Philadelphia, Pennsylvania 19104–6323, USA*

[2]*Department of Materials and Interfaces, Weizmann Institute of Science, Rehovot 76100, Israel*[†]

[3]*Department of Chemistry, Northwestern University, Evanston, Illinois 60208, USA*

[4]*Max Planck Institute for Solid State Research, Stuttgart 70569, Germany*

[5]*University of Crete, Heraklion, Greece*

(Dated: June 10, 2021)

* omer.yaffe@weizmann.ac.il

† These authors contributed equally

SUPPORTING INFORMATION

Synthesis methods

$CsPbBr_3$ single crystals were synthesized using solution method discussed in Ref[S1]. $CsSnBr_3$ was prepared by method used in Ref[S2]. For the preparation of $CsGeBr_3$, 9 mL of HBr (48%, ACS reagent grade, Sigma Aldrich) was diluted with 4.5 mL of deionized water, then GeO_2 (0.315 g or 3 mmol, Sigma Aldrich) was added to the solution under stirring at 150 °C. 3 mL of H_3PO_2 (50%, Sigma Aldrich) was added as a reducing agent, after approximately 30 minutes the GeO_2 was fully dissolved and reduced to $GeBr_2$, resulting in a colorless solution. Upon addition of CsBr (0.638 g or 3 mmol, 99.999%, Sigma Aldrich) to this clear solution, small crystals of the bright yellow product immediately precipitate. Once the solution had cooled to room temperature, the product was filtered under vacuum and dried under vacuum for an additional 3 hours. Yield of the reaction was about 90%.

Experimental details

Temperature-dependent, low-frequency micro-Raman scattering measurements were performed in a customized set-up as discussed in [S3,S4]. Briefly, all the samples were excited with 1.16 eV radiation from a linearly polarized, Nd:YAG solid state laser (Coherent inc., USA). 1.16 eV energy falls in the below bandgap region of all the samples used, which helps to avoid the damage due to absorption of bandgap radiation.

Polarized Raman configuration was used to overcome the dependence of Raman scattering on the direction of laser polarization and the crystallographic orientation of the measured crystal. In polarized configuration, Raman spectra was acquired for several angles of incident polarization (from $\theta = 0 - 360°$) with respect to an arbitrary crystallographic axis. Rotation of polarization was achieved using a motorized zero-order half-wave plate (Thorlabs, USA) in the incident beam direction, which rotated with small increments (10°) between successive Raman measurements. The back-scattered beam was filtered either parallel or perpendicular to the incident polarization using another polarizer (called analyser).

The individual spectra at each angle of polarization (for both parallel and perpendicular configuration) were then summed and normalized to obtain an unpolarized spectrum. The advantage of using polarized Raman and subsequent averaging and normalization is two-

fold: (1) It results in an equivalent unpolarized (isotropic) spectrum and makes all Raman active-modes or features visible at the same time regardless their symmetry. (2) Notably, it is quite difficult to obtain all the crystals with the same orientation since different crystals have different preferential orientation during synthesis. Thus, our normalization procedure helps to normalize the effect of preferential orientations of the different measured crystals and makes a legitimate comparison between $CsPbBr_3$, $CsSnBr_3$ and $CsGeBr_3$ possible. The Raman spectra presented in Fig. 2 and Fig. 3 are averaged over both parallel and perpendicular configurations.

Fitting Procedure

Each averaged experimental Raman spectrum in cubic phase was deconvolved to a product of the Bose-Einstein distribution (n_{BE}) and multi-Lorentz line shape using the procedure used in Ref[S3,S5]. Notably, the deconvolution of the Raman spectrum of $CsSnBr_3$ crystal at 80 K required a Debye relaxational component in addition to the Lorentz oscillator model. The experimentally measured Raman spectrum is expressed as a combination of Debye and a damped Lorentz oscillator term (eq. S1).

$$I_{exp}(\nu, \nu_i, \Gamma_i) = c_{BE}(\nu) \left(\frac{c_0 |\nu| \Gamma_0}{\nu^2 + \Gamma_0^2} + \sum_{i=1}^{n} c_i \frac{|\nu||\nu_i|\Gamma_i^2}{\nu^2\Gamma_i^2 + (\nu^2 - \nu_i^2)^2} \right), \tag{S1}$$

where ν is the spectral shift, ν_is are the resonance energies of the Lorentz oscillators, Γ_0 and Γ_i are the damping coefficients of the Debye relaxation and Lorentz oscillators respectively, c_0 and c_is are unitless fitting parameters for the intensities of the Debye and Lorentz oscillator components respectively. The spectral shift ν, the parameters ν_i and Γ_i are in wavenumber units. The approximate lifetime of the phonons can be calculated as $\tau = \frac{1}{2\pi c \Gamma_i}$, where c is the speed of light. $c_{BE}(\nu)$ includes the Bose-Einstein distribution of thermal population where

$$c_{BE}(\nu) = \begin{cases} n_{BE} + 1 & \text{for Stokes scattering,} \\ n_{BE} & \text{for Anti-Stokes scattering.} \end{cases}$$

with n being the Bose-Einstein distribution. The spectral artifacts due to the notch filter around 0 cm^{-1} were omitted and only the Stokes scattering was fitted to find the positions

and widths of the peaks. The fitting was carried out in the customized MATLAB code and Igor Pro 8.

The Raman features in the higher temperature, cubic data were heavily damped to produce a good overall fit containing the central peak (peak closest to 0 cm^{-1}). The Γ_i values obtained from fitting were used to calculate the lifetime of the Raman modes. The calculated lifetimes for the central peak corresponding to $CsPbBr_3$, $CsSnBr_3$ and $CsGeBr_3$ are $\approx$ 180 fs, 162 fs and 255 fs respectively.

TABLE S1. Fit position and width parameters for cubic phase from fits of Raman data to Eq. 1.

$CsPbBr_3$		$CsSnBr_3$		$CsGeBr_3$	
ω (cm^{-1})	Γ (cm^{-1})	ω (cm^{-1})	Γ(cm^{-1})	ω (cm^{-1})	Γ (cm^{-1})
25.1	28.0	25.0	32.7	22.6	20.8
40.0	34.8	70.0	82.7	47.1	51.3
73.0	40.0	149.7	150.0	83.9	53.6
164.1	148.8	-	-	148.7	54.1
-	-	-	-	176.3	32.9

TABLE S2. Fit position and width parameters for orthorhombic phase from fits of Raman data to Eq. 1.

$CsPbBr_3$		$CsSnBr_3$	
ω (cm^{-1})	Γ (cm^{-1})	ω (cm^{-1})	Γ(cm^{-1})
28.2	1.6	21.2	3.6
30.8	2.4	27.0	5.7
32.5	1.7	28.2	3.3
36.9	1.7	40.6	4.2
42.2	1.1	44.5	2.0
46.3	1.1	58.0	6.2
49.0	2.3	72.0	8.8
67.3	1.6	77.6	4.0
71.0	2.5	-	-
73.9	2.4	-	-
80.2	1.9	-	-
130.0	4.2	-	-

Inadequacy of Ionic Size Models

$CsPbBr_3$ transforms from the cubic perovskite to a tetragonal tilted phase at 403 K, and then to an orthorhombic phase characterized by $a^+b^-b^-$ tilting in Glazer notation at 361 K.[S6] For $CsSnBr_3$, reports conflict about the intermediate temperature phase evolution but are in agreement that the cubic phase transforms just below room temperature to one or more tetragonal phases, followed by the same $a^+b^-b^-$ tilting pattern to orthorhombic structure at ≈250 K.[S2,S7–S9] $CsGeBr_3$ transforms on cooling from the cubic phase at 511 K to a rhombohedral phase characterized by ferroic displacements of Ge^{2+} along the [111] cubic direction.[S10]

We construct 2D structural map with tolerance factor t and octahedral factor μ based on previous studies to describe the formability of halid perovskites[S11,S12] in Fig. S1(a). For the light purple pentagon[S12], the leftmost boundary represents tilt limit, beyond which the pervoskite network will collapse into edge-sharing or face-sharing octahedra. The rightmost vertical line represents the stretch limit $t = 1$, and when $t < 1$, the corner-sharing octahedra have a tilting tendency. The top-right line represents the upper bound of r_A/r_X, determined by the largest A cation and the smallest anion. The top-horizontal line represents the upper bound of r_B/r_X, determined by the largest B cation and the smallest X anion. Two dashed lines are derived from Pauling's first rule[S13], which tells the range of μ based on the geometric configuration and the coordination number of anions. For octahedron with coordination number 6, $\sqrt{2} - 1 < \mu < \sqrt{3} - 1$[S14], and the lower dashed line overlaps with the bottom of the pentagon. For the light green rectangle[S11], the boundary is established upon the classification of pervoskites and non-perovskites for 186 halide systems at ambient temperature and pressure according to empirical parameters .

As shown in the $t-\mu$ structural map (Fig. S1(a)), $CsPbBr_3$ (t=0.86, μ=0.61) and $CsSnBr_3$ (t=0.92, μ=0.51) both lie squarely in the region of expected perovskite formation. However, $CsGeBr_3$ (t=1.01, μ=0.37) sits just outside the window of expected perovskite formation, but forms a polar, rhombohedrally distorted perovskite with no octahedral tilting (the structure of the ground state of $BaTiO_3$). The [111] Ge^{2+} displacements simultaneously lead to a favorable coordination (3 short bonds, 3 long bonds) where the lone pair is stereochemically expressed in the opposite direction (along $[\bar{1}\bar{1}\bar{1}]$) and the rhombohedral stretching of the lattice expands the A-site cage, accommodating the large Cs^+ cation. The small μ, large

t, and strong lone-pair driven distortion for Ge–Br bonds conspire to stabilize the distorted perovskite structure. Therefore, the ionic size effect is insufficient to qualitatively rationalize the reported structure evolution with temperature. and covalency must be taken into account.

Apart from $CsGeBr_3$, the crystal structures of several compounds highlighted in Fig.S1(a) as failures of the ionic size model (Goldschmidt's tolerance factor t+ octahedral factor μ) are given in Fig.S1(b)(c), illustrating the important role of covalency in structure and dynamics. $CsPbF_3$ (t=0.90, μ=0.89) has such a high octahedral factor (Pb^{2+} is large with respect to F^-) that it might be expected to adopt a different structure type with a higher coordination number for Pb. Instead, it is reported to transform from a cubic perovskite at 187 K to a polar ground state that combines tilting and lone pair-driven intra-octahedral distortions (the $LiNbO_3$ structure).[S15] Such crystallographic coexistence of tilting and intra-octahedral distortions is somewhat rare because tilting reduces the driving force for lone pair stereochemical activity via its effects on bond angles and orbital overlap, but is also reported (with different tilting patterns and displacement directions) for $RbGeBr_3$[S16] and $CH_3NH_3SnBr_3$.[S17] $CsSnCl_3$ (t=0.93, μ=0.55) would be strongly expected to form a perovskite on the basis of size but rather exists as a salt of Cs^+ and $(SnCl_3)^-$ pyramidal anions at room temperature because of strong lone pair-driven distortions.[S18]

The tendency for lone-pair-driven distortion is stronger for lighter cations[S19]. We illustrate the lone-pair stereochemcial activity by plotting the electron localization functions of three compounds in Fig. S2. Structures are chosen from molecular dynamics trajectories at different times. Clearly asymmetric and separate lobes are formed at locations opposite to the cation displacements. The charge localization effect is more significant in $CsSnBr_3$ and $CsGeBr_3$.

Computational Methods

We performed Born-Oppenheimer AIMD with the Quantum-ESPRESSO code[S20], and we used the GGA functional[S21]. A $2\times2\times2$ supercell containing eight formula units of $CsMBr_3$ was chosen for cubic phase and a $\sqrt{2}\times2\times\sqrt{2}$ supercell containing 4 formula units was chosen for orthorhombic phase. A $3\times3\times3$ k-point grid was used for the cubic supercell, and a $4\times3\times4$ k-point grid was used for the orthorhombic supercell. The plane-wave cutoff energy

was set to 55 Ry. The DFT total energy was converged to 10^{-7} Ry/cell. To compare with experiments, at cubic phase AIMD was performed at 500 K, 330 K and 663 K for $CsPbBr_3$, $CsSnBr_3$ and $CsGeBr_3$ respectively. At orthorhombic phase, AIMD was performed at 80 K. The time step of AIMD was set to 10 fs. We equilibrated the systems with Andersen thermostat for 10 ps, and run another 50 ps to obtain a converged autocorrelation function. To obtain the Raman spectra, density functional perturbation theory (DFPT) was used to calculate the polarizability for selected structures[S22]. Density functional perturbation theory (DFPT) was also applied on one primitive cell to calculate the phonon dispersion about orthorhombic structures, with a $3 \times 2 \times 3$ k-point grid and 10^{-16} Ry/cell as the converged energy criterion.

The autocorrelation function of the polarizability tensor approach was employed to compute Raman activities[S23]. Polarizabilities of selected structures were obtained from the ab-initio molecular dynamics (AIMD) trajectory at an interval of 80 fs, and we employed the Wiener-Khintchine's theorem to calculate the autocorrelation functions[S24,S25].

We calculated frequency-filtered trajectories first by performing a Fourier transformation on the real-space MD trajectories (from t to ω), and then filtered the ω-space trajectories within a frequency window $\Delta\omega(\pm 5\ \mathrm{cm}^{-1})$, and finally performed an inverse Fourier transform back to t. The whole procedure is expressed as:

$$\vec{R}_{\mathrm{filtered}}(t;\omega_0)=$$

$$\mathcal{F}^{-1}\left[\Theta\left(\omega-(\omega_0-\Delta\omega)\right)\Theta\left(-\omega+(\omega_0+\Delta\omega)\right)\mathcal{F}\left[\vec{R}(t)\right]\right]. \tag{S2}$$

The projection is defined as:

$$W_{\vec{u},\omega}=\frac{1}{N_t}\sum_t \frac{|\vec{R}_{\mathrm{filtered}}(t;\omega)\cdot\vec{u}\,|^2}{|\,\vec{R}\,|^2(t;\omega)}, \tag{S3}$$

where $\vec{R}_{\mathrm{filtered}}(t;\omega)$ is the frequency-filtered trajectory, regarded as the ω-component of real atomic MD trajectories. $3N$ of $\vec{u}$ are established as a complete basis to describe the atomic motion, where N is the number of atoms in the simulation cell. Since we focus on capturing different structural instabilities, we classify $\{\vec{u}\}$ into 5 categories: (1) Cs motion; (2) M motion; (3) Br_6 tilting motion; (4) Br stretching motion; (5) distortion motion (deformation of Br_6 octahedra). All motions are illustrated in Fig. S3. With the weight $W_{\vec{u},\omega_0}$ of each

component, we can tell the specific motions corresponding to the Raman spectral weight at frequency ω_0.

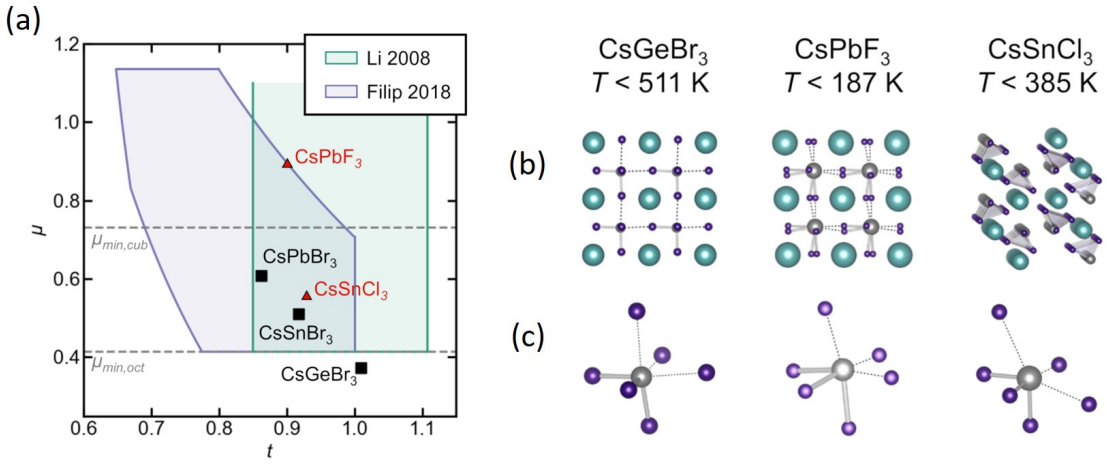

FIG. S1. (a) Regions of perovskite formability based on ionic size ratios[S11,S12] and the minimum radius ratios for octahedral ($\mu_{min,oct}$) and cubic ($\mu_{min,cub}$) coordination from Pauling's first rule. The locations of the compounds under study are overlaid (black squares). Red triangles indicate notable failures of this geometric model. Several halides whose structures are incorrectly predicted on the basis of ionic sizes alone. (b) Crystal structures and (c) dication coordination environments for the low temperature phases of $CsGeBr_3$,[S10] $CsPbF_3$,[S15] and $CsSnCl_3$.[S18]

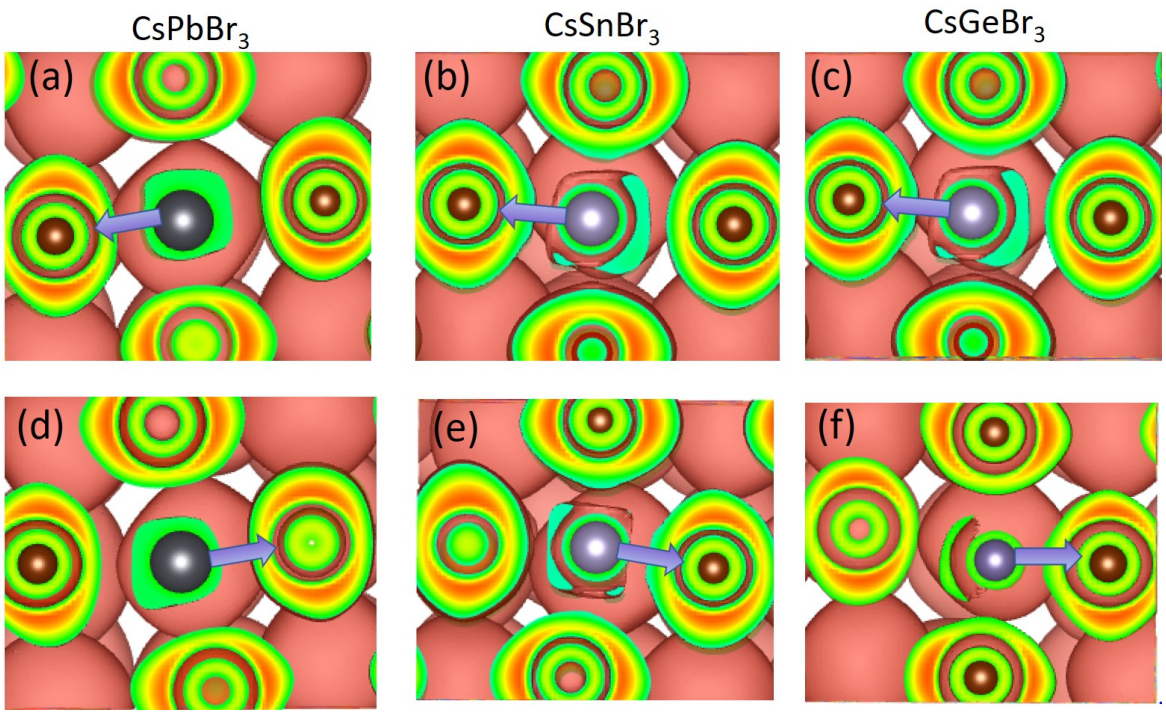

FIG. S2. Electron localization function (ELF) plot to illustrate lone pair stereochemical activity in $CsPbBr_3$, $CsSnBr_3$ and $CsGeBr_3$. The ELF levels are 0.4 for $CsGeBr_3$ and 0.3 for $CsSnBr_3$ and $CsPbBr_3$. M (M = Pb, Sn, Ge) atom is the grey ball in the center and four Br atoms are brown balls around M atom. The arrow denote the direction of the displacement of M cation. Upper Panel is when M atom moves towards the left Br atom and Lower Panel is when M atom moves towards the right Br atom. Displacements relative to initially high-symmetry positions are 0.17 Å, 0.15 Å and 0.24 Å for for Pb, Sn and Ge, respectively.

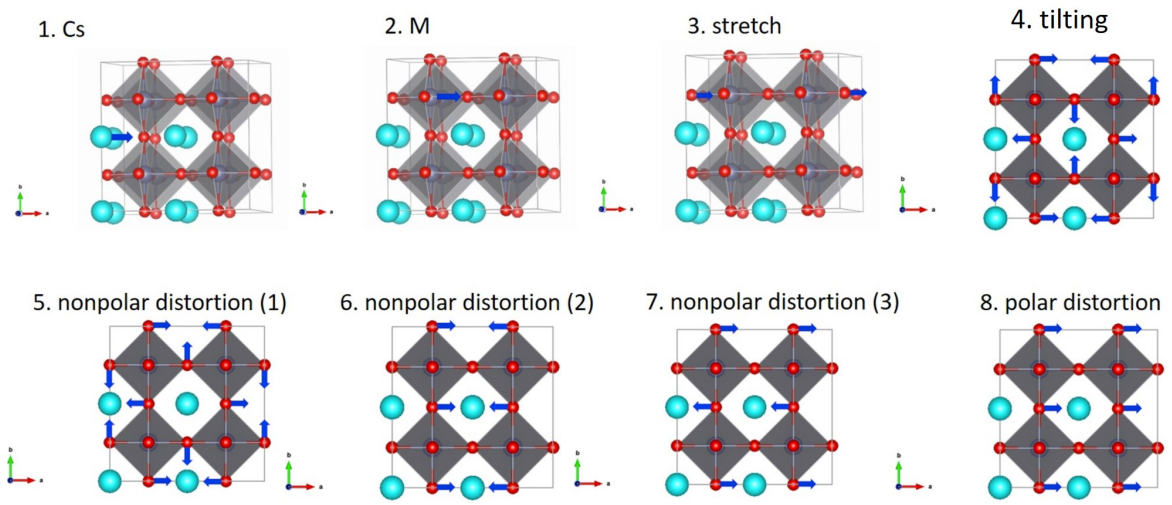

FIG. S3. Illustration for self-defined 120 motions in $2\times2\times2$ supercell. There are 24 Cs motions, 24 M motions, 24 stretch motions, 6 tilting motions, 6 type (1) nonpolar distortion motions, 12 type (2) nonpolar distortion motions, 12 type (3) nonpolar distortion motions,and 12 poloar distortion motions.

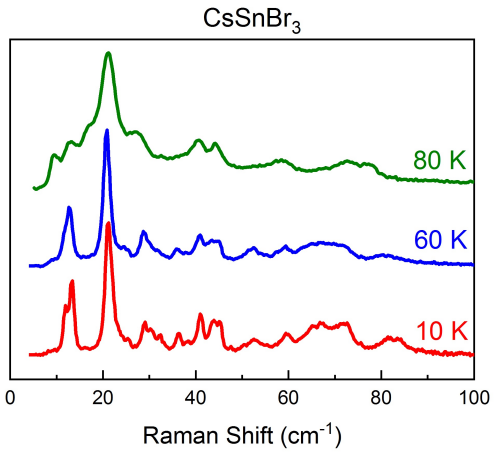

FIG. S4. Raman spectra indicating phase change in $CsSnBr_3$ below 80 K.

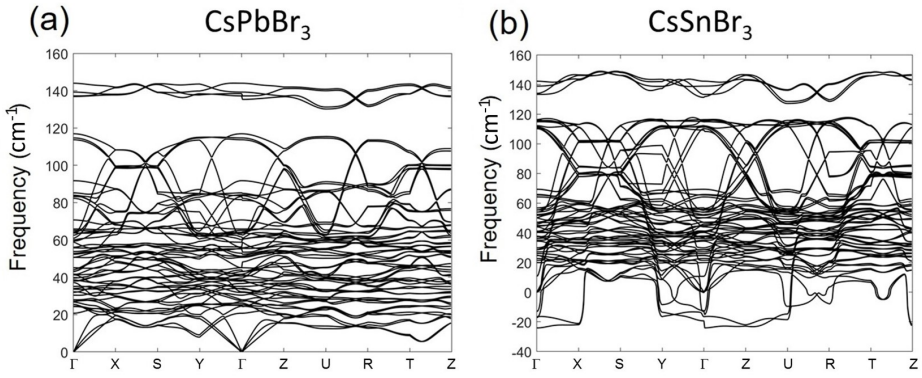

FIG. S5. 0 K, DFT phonon dispersion relations for the orthorhombic phases of (a) $CsPbBr_3$ and (b) $CsSnBr_3$. Several phonon modes with imaginary frequencies down to $20i$ cm^{-1} at high-symmetry points Γ, R, T, U, X, Y, Z demonstrate that the orthorhombic structure of $CsSnBr_3$ is unstable.

[S1] C. C. Stoumpos, C. D. Malliakas, J. A. Peters, Z. Liu, M. Sebastian, J. Im, T. C. Chasapis, A. C. Wibowo, D. Y. Chung, A. J. Freeman, B. W. Wessels, and M. G. Kanatzidis, Cryst. Grow. Des. **13**, 2722 (2013).

[S2] D. H. Fabini, G. Laurita, J. S. Bechtel, C. C. Stoumpos, H. A. Evans, A. G. Kontos, Y. S. Raptis, P. Falaras, A. Van der Ven, M. G. Kanatzidis, and R. Seshadri, J. Am. Chem. Soc. **138**, 11820 (2016).

[S3] R. Sharma, M. Menahem, Z. Dai, L. Gao, T. M. Brenner, L. Yadgarov, J. Zhang, Y. Rakita, R. Korobko, I. Pinkas, *et al.*, Physical Review Materials **4**, 051601 (2020).

[S4] R. Sharma, Z. Dai, L. Gao, T. M. Brenner, L. Yadgarov, J. Zhang, Y. Rakita, R. Korobko, A. M. Rappe, and O. Yaffe, Phys. Rev. Mater. **4**, 092401 (2020).

[S5] M. Asher, D. Angerer, R. Korobko, Y. Diskin-Posner, D. A. Egger, and O. Yaffe, Advanced Materials **32**, 1908028 (2020).

[S6] S. Hirotsu, J. Harada, M. Iizumi, and K. Gesi, J. Phys. Soc. Japan **37**, 1393 (1974).

[S7] M. Mori and H. Saito, J. Phys. C Solid State Phys. **19**, 2391 (1986).

[S8] M. H. Kuok, E. L. Saw, and C. T. Yap, Phys. status solidi **132**, K89 (1992).

[S9] D. E. Scaife, P. F. Weller, and W. G. Fisher, J. Solid State Chem. **9**, 308 (1974).

[S10] G. Thiele, H. W. Rotter, and K. D. Schmidt, Z. Anorg. Allg. Chem. **545**, 148 (1987).

[S11] C. Li, X. Lu, W. Ding, L. Feng, Y. Gao, and Z. Guo, Acta Crystallogr. Sect. B **64**, 702 (2008).

[S12] M. R. Filip and F. Giustino, Proc. Natl. Acad. Sci. **115**, 5397 LP (2018).

[S13] L. PAULING, J. Am. Chem. Soc. **51**, 1010 (1929).

[S14] G. S. Rohrer, *Structure and bonding in crystalline materials* (Cambridge University Press, 2001).

[S15] P. Berastegui, S. Hull, and S.-G. Eriksson, J. Phys. Condens. Matter **13**, 5077 (2001).

[S16] G. Thiele, H. Rotter, and K. Schmidt, Zeitschrift für anorganische und allgemeine Chemie **559**, 7 (1988).

[S17] I. Swainson, L. Chi, J.-H. Her, L. Cranswick, P. Stephens, B. Winkler, D. J. Wilson, and V. Milman, Acta Crystallographica Section B: Structural Science **66**, 422 (2010).

[S18] F. R. Poulsen and S. E. Rasmussen, Acta Chem. Scand. **24**, 150 (1970).

[S19] U. V. Waghmare, N. A. Spaldin, H. C. Kandpal, and R. Seshadri, Phys. Rev. B **67**, 125111 (2003).

[S20] P. Giannozzi, S. Baroni, N. Bonini, M. Calandra, R. Car, C. Cavazzoni, D. Ceresoli, G. L. Chiarotti, M. Cococcioni, I. Dabo, A. D. Corso, S. de Gironcoli, S. Fabris, G. Fratesi, R. Gebauer, U. Gerstmann, C. Gougoussis, A. Kokalj, M. Lazzeri, L. Martin-Samos, N. Marzari, F. Mauri, R. Mazzarello, S. Paolini, A. Pasquarello, L. Paulatto, C. Sbraccia, S. Scandolo, G. Sclauzero, A. P. Seitsonen, A. Smogunov, P. Umari, and R. M. Wentzcovitch, J. Phys.: Condens. Matter **21**, 395502 (1 (2009).

[S21] J. P. Perdew, K. Burke, and M. Ernzerhof, Phys. Rev. Lett. **77**, 3865 (1 (1996).

[S22] X. Gonze and C. Lee, Phys. Rev. B **55**, 10355 (1997).

[S23] M. Thomas, M. Brehm, R. Fligg, P. Vöhringer, and B. Kirchner, Physical Chemistry Chemical Physics **15**, 6608 (2013).

[S24] N. Wiener *et al.*, Acta mathematica **55**, 117 (1930).

[S25] A. Khintchine, Mathematische Annalen **109**, 604 (1934).